





Impacts of distorted local chemical coordination on electrochemical performance in hydrated vanadium pentoxide

Received: 17 April 2024

Accepted: 21 October 2024

Published online: 31 October 2024


 Check for updates

Huanhuan Niu¹, Heng Liu¹, Long Yang¹ , Te Kang¹, Ting Shen², Bingqi Jiang¹, Wei-Hsiang Huang³ , Chun-Chi Chang⁴, Yanzhong Pei¹  , Guozhong Cao⁵  & Chaofeng Liu¹  

Modulating and elevating the operating voltage of a given cathode is a significant challenge to enhance the energy density of secondary batteries without sacrificing power output. The chemical coordination strongly influences the energy levels of *d*-orbitals of redox cations in cathode materials, which tie to their operating voltage. In contrast to concentrated studies on enhancing the specific capacity, in this study, we choose bi-layered hydrated vanadium pentoxide as the model to modulate the *d*-orbital energy levels through local chemical coordination manipulation, achieving a higher operating voltage in rechargeable aqueous zinc ion batteries. Here we show that, by employing X-ray absorption spectroscopy (XAS) and pair distribution function (PDF) techniques, we can analyze the distortion of [VO₆] octahedra and extract chemical bond information, deciphering the correlation between the chemical coordination and operating voltage in cathode materials. The fundamentals could guide the designing and developing RAZIBs with higher energy and power density.

Rechargeable Aqueous Zn-ion batteries (RAZIBs), as one of the multi-valent ion batteries, have garnered widespread attention due to their high safety, low cost, and environmental friendliness. These characteristics make them a highly promising candidate in next-generation efficient rechargeable batteries^{1–3}. Given the high theoretical specific capacity (820 mA h g⁻¹ and 5855 mA h cm⁻³) and relatively low electrochemical potential (−0.76 V vs. Standard Hydrogen Electrode) of zinc anode, developing matchable cathodes with higher operating voltage and accelerated ion diffusion has become a critical challenge, which impedes the practical applications^{4,5}. In the past, a variety of

materials have been developed to serve as the high-specific capacity cathodes for RAZIBs, including manganese-based oxides⁶, Prussian blue analogues⁷, polymers⁸, and vanadium-based compounds^{9,10}. However, scarce studies focus on the electrochemical potential of the electrode materials and decipher its determinators, especially the functions of the local chemical coordination and crystal field. Generally, redox ions and their coordination build structural units such as octahedra and tetrahedra to influence the configuration/occupation characteristics of *d*-orbitals participating into redox reaction¹¹. Therefore, addressing the urgent challenges of manipulating the

¹Interdisciplinary Materials Research Center, School of Materials Science and Engineering, Tongji University, Shanghai 201804, China. ²Department of Materials Science and Engineering, Clemson University, Clemson, SC 29634, USA. ³National Synchrotron Radiation Research Center (NSRRC), Hsinchu 300092, Taiwan. ⁴Graduate Institute of Applied Science and Technology, National Taiwan University of Science and Technology, Taipei 10607, Taiwan. ⁵Department of Materials Science and Engineering, University of Washington, Seattle, WA 98195, USA.  e-mail: yanzhong@tongji.edu.cn; gzcao@uw.edu; chaofeng@tongji.edu.cn

coordination environment of redox ions and exploring the correlations between the d -orbitals and electrochemical potential is crucial for developing high-energy density RAZIBs.

Hydrated vanadium pentoxide ($V_2O_5 \cdot nH_2O$, VOH) has a bi-layered crystal structure with variable chemical states, offering high specific capacity and regulable structure characteristics¹². Strategies have been explored to improve the comprehensive electrochemical performance of VOH, such as the doping of alien cations¹³, the incorporation of conductive polymers^{14–17} and the application of surface coating¹⁸. In particular, pre-intercalation, which involves the insertion of foreign guests into the host lattice, has demonstrated considerably effective way of regulating the chemical coordination environment¹⁹. With either individual or joint pre-intercalating of metal ions²⁰, non-metal ions/molecules, and organic compounds²¹, the performance of pre-intercalated cathode could experience significant enhancements due to the expanded interlayer spacing²², shielded electrostatic interaction between the charge carriers and the lattice oxygen²³, and enhanced electrical conductivity²⁴. The bulk of these studies concentrate on fast mass transfer to achieve a greater specific capacity and improved rate performance. However, the correlations between the local changeable chemical coordination and the enhanced electrochemical potential in detail are unclear and need to be explored carefully, especially the changes on the electrochemical potentials of VOH.

In this work, we propose that manipulating the coordination environment in VOH alters the V $3d$ orbital configurations, thereby

modulating the electrochemical potential. Thus, organic cations pre-intercalated VOH are synthesized by a facile hydrothermal reaction with choline and derivatives as the additives to induce the $[VO_6]$ octahedra distortion and V $3d$ orbitals splitting. The sample with greater distortion achieves a higher operating voltage and rapid ion migration together in RAZIBs. By employing X-ray absorption spectroscopy (XAS) and pair distribution function (PDF), the local coordination environment distortions were analyzed to decipher the relationship between the coordination environment, electronic configurations, and electrochemical performance. This work provides guidance for the design and development of vanadium oxides with high voltage and rapid ion diffusion for high-performance RAZIBs.

Results and discussion

Structure and chemical states

The samples were synthesized through a hydrothermal method and the details are described in the method section. The samples with intercalated choline ($C_5H_{13}N^+OH$, Ch) and chlorcholine ($C_5H_{13}N^+Cl$, Ch_2) cations are denoted as Ch-VOH and Ch_2 -VOH, respectively. Figure 1a presents the XRD patterns of Ch_2 -VOH and Ch-VOH, and the strongest peak locates at 6.76° in Ch_2 -VOH associating to the (001) plane with the lattice spacing of 13.1 \AA . In contrast, the (001) plane diffraction peak of Ch-VOH appears at $2\theta = 6.8^\circ$, indicating a lattice spacing of 12.9 \AA . The lattice spacings of (001) plane of both samples exhibit an increase compared to 11.5 \AA of pristine VOH (JCPDS

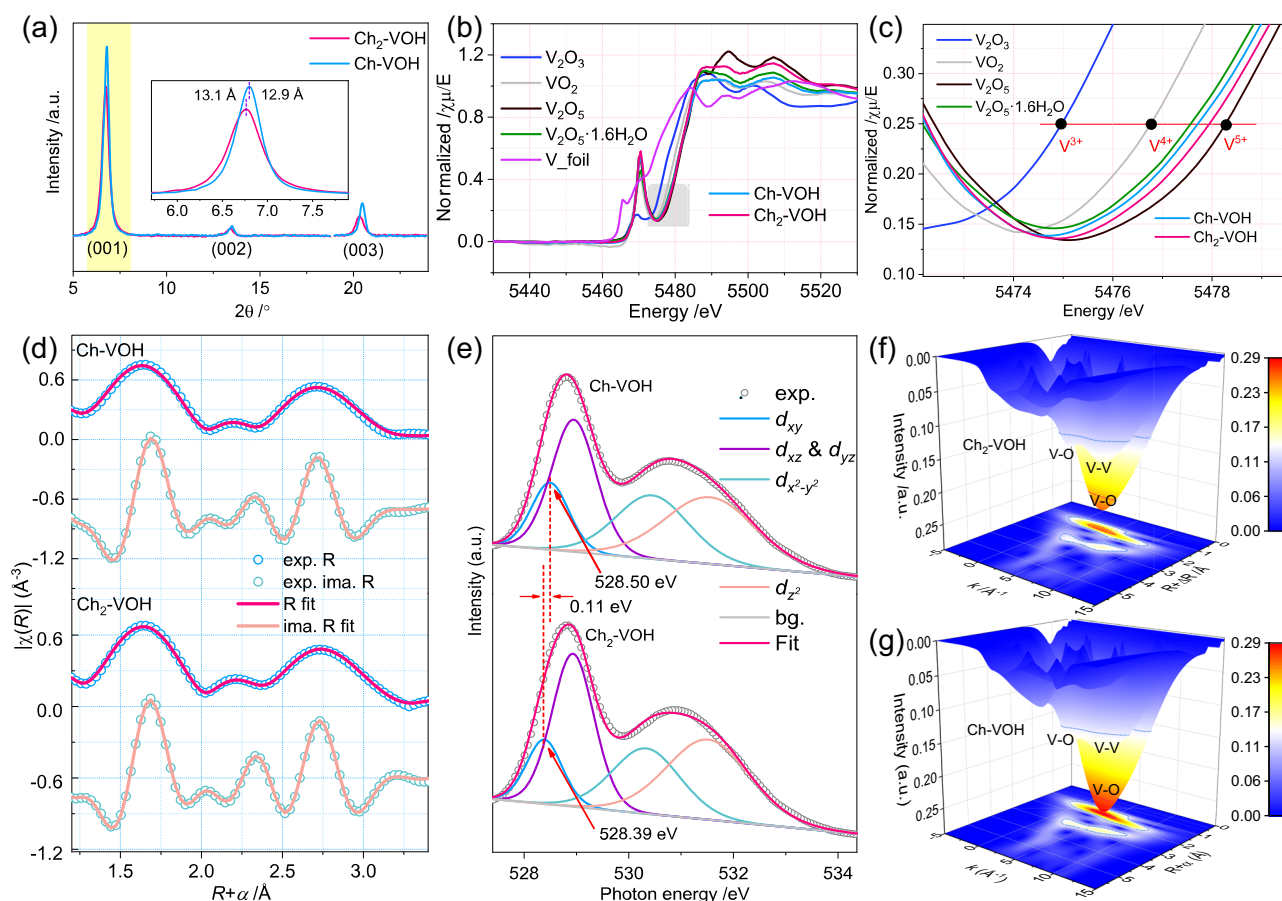


Fig. 1 | Structure information of Ch_2 -VOH and Ch-VOH. **a** XRD patterns. Both samples have the same crystal structure but different spacing distances of (001) crystal plane. **b** The V K-edge XAS spectra of V foil and V oxides with different oxidation states. The pre-edge peak reflects the octahedra distortion and the $1s \rightarrow 3d$ electron hopping, the near edge presents the chemical states of V in the different chemical surroundings. **c** The enlarged image of absorption edge from

Fig. b. The change in oxidation state is reflected by the almost 3 eV difference in rising edge energies between V_2O_3 and V_2O_5 . **d** V K-edge EXAFS (point) of Ch-VOH and Ch_2 -VOH and their fitting curves (line) in R -space. The data are k^2 -weighted without phase-corrected. **e** O K-edge soft XAS spectra of Ch-VOH and Ch_2 -VOH. The corresponding wavelet transform diagrams of (f) Ch-VOH and (g) Ch_2 -VOH. The V-O chemical coordination have changed in the ab plane of the octahedra.

40-1296)²⁵. This observation is further corroborated by the HRTEM images presented in Supplementary Fig. 1. The results from the energy dispersive X-ray spectrometer (EDS) mapping reveal that the chlorine (Cl) signal was exclusively detected in Ch₂-VOH, demonstrating a discrepancy in the pre-inserted cations. In the electron paramagnetic resonance (EPR) spectra, both Ch₂-VOH and Ch-VOH exhibit symmetric signals at g value = 2.003 (Supplementary Fig. 2a). These signals correspond to unpaired electrons captured at the oxygen vacancies²⁶, providing further evidence of the successful pre-insertion of organic cations. Raman spectra in Supplementary Fig. 2b display four peaks at approximately 990, 690, 406, and 281 cm⁻¹ in both samples. These peaks correspond to the stretching vibration of V=O (990 cm⁻¹) and V₂O (690 cm⁻¹), respectively, as well as the bending vibration of V=O (406 and 281 cm⁻¹)²⁰. Fourier transform infrared (FTIR) spectra in Supplementary Fig. 2c identify that the peaks around 738, 978 and 1005 cm⁻¹ represent the characteristic bands of vanadium oxide framework²⁷. The peak observed at around 738 cm⁻¹ is associated with the stretching vibrations of V-O-V. Meanwhile, the peaks appeared near 1005 and 978 cm⁻¹ are attribute to V=O, which is split into two peaks corresponding to the stretching vibration of V⁵⁺=O and V⁴⁺=O, respectively²⁸. The peak located around 1623 cm⁻¹ in Ch-VOH corresponds to the bending vibration of H-O-H. However, the absence of a distinct bending vibrational peak at the same position in Ch₂-VOH indicates that it contains less interlayer water compared to Ch-VOH. In the thermogravimetric analysis - differential scanning calorimetry (TG-DSC) curves (Supplementary Fig. 3), the amounts of pre-inserted cations C₅H₁₃N⁺Cl and C₅H₁₃N⁺OH are nearly identical, approximately 9.0 and 9.1 wt %, respectively. After heating to 350 °C, Ch-VOH exhibits a lower residual mass, corroborating the presence of more interlayer water in Ch-VOH. In addition, a vibrational peak belonging to -OH is observed around 1414 cm⁻¹ only in the Ch-VOH spectrum, further confirming the difference in pre-inserted cations for both samples. Figure 1b, c shows the V K-edge X-ray absorption spectroscopy (XAS) spectra of Ch₂-VOH and Ch-VOH. Notably, the pre-edge peak corresponds to 1s to 3d electronic transition, demonstrating high sensitivity to the crystal field symmetry as well as to the electron occupied state of the V 3d orbitals. According to the dipole forbidden principle, the intensity of pre-edge peaks for both samples should be weak or undetected. On the contrary, the pre-edge peak intensities of the samples are strong, indicating the occurrence of orbital hybridization between the O 2p and V 3d orbitals²⁹. The increase in pre-edge peak intensity from Ch-VOH to Ch₂-VOH suggests an increase in the number of 3d unoccupied orbitals and a greater level of orbital hybridization between O 2p and V 3d orbitals in Ch₂-VOH. Additionally, the findings indicate that the pre-intercalation of C₅H₁₃N⁺Cl induce greater distortion of [VO₆] octahedra³⁰. Furthermore, the main absorption edges of Ch-VOH and Ch₂-VOH also confirm that V in Ch₂-VOH processes a higher oxidation state (Fig. 1c).

The K²-weighted Fourier transforms of the V K-edge extended X-ray absorption fine structure (EXAFS) and the corresponding fitting curves simulated by Artemis³¹ provide the coordination information of the central atoms (Fig. 1d, e). The fitting on R space of both samples adopt identical structure (Supplementary Fig. 4a) without phase-correction. The slabs of V₂O₅ bilayers are separated by water molecules and stacked along the c -axis. It has a monoclinic unit cell (space group C2/m) with parameters $a = 11.722(3)$ Å, $b = 3.570(3)$ Å, $c = 11.520(3)$ Å, and $\beta = 88.65^\circ$. The stacking sequence shows signatures of turbostratic disorder and a structural coherence limited to 50 Å³², and the parameters are detailed in the Supplementary Table 1. The radial structure functions corresponding to the central absorption vanadium atom emphasize that the interlayer spacing increases and the distance from oxygen located at the vertex to vanadium become short after the cation pre-intercalation. The peak at 1.1 Å originates from the single scattering contribution of oxygen along the c -axis (Supplementary Fig. 6). Peak at 1.6 Å corresponds to the cooperative scattering from

the four O atoms at the equator within the [VO₆] octahedra³³. The octahedral crystal field distortion caused by the pre-inserted will lead to a secondary splitting of the 3d orbitals. Compared to Ch-VOH, there are more shorter V-O along the c -axis in Ch₂-VOH (Supplementary Tables 2, 3). This results in a greater crystal field repulsion along the c -axis in Ch₂-VOH. In addition, the peak at around 2.8 Å arises from scattering contributions of V-V between adjacent octahedra. Note that the radial distance of V-V in both samples remains unchanged before and after intercalation, suggesting a rigid and stable framework in the whole host structure. The V L-edge and O K-edge soft XAS of Ch-VOH, Ch₂-VOH, and VOH are presented in Fig. 1e and Supplementary Fig. 7. The V L-edge spectra (Supplementary Fig. 7a) correspond to dipole selection rules that permit transitions from a defined ground state ($2p^63d^n$) to a potential final state ($2p^53d^{n+1}$). The spectra display two peaks around 518 eV and 525 eV, which can be attributed to the $2p_{3/2}$ and $2p_{1/2}$ energy levels, respectively. The O K-edge spectra represent transitions from the O core level to the unoccupied conduction band that hybrids with O 2p states. Different features in the spectra primarily correspond to bands of metal orbital energy levels. The prominent doublets around 528–537 eV are attributed to V 3d bands split by the crystal field effect. The doublet splitting in the spectra provides detailed information about V 3d bands, which can be explained qualitatively in terms of symmetry³⁴. As shown in Supplementary Tables 2, 3, the shortest V-O bond in Ch₂-VOH has a higher coordination number compared to Ch-VOH, leading to larger secondary splitting of the t_{2g} orbitals³⁵. Consequently, the d_{xy} orbital of Ch₂-VOH has a lower energy level than that of Ch-VOH. The corresponding wavelet transform diagrams in Fig. 1f, g reveal that the strongest peaks stem from the V-O single scattering contribution (1st coordination sphere), and the other peaks correspond to the V-V (2nd sphere), and V-O (3rd sphere) scattering contribution, respectively.

Furthermore, the synchrotron X-ray atomic pair distribution function (PDF) analysis is performed on these samples. The PDF fits are performed over two different regions, i.e., 1.2 to 11.5 Å for intralayer structure modeling (Fig. 2a–d), and 1.2 to 21.0 Å for interlayer structure modeling (Supplementary Fig. 9), and detailed parameter values are reported in Supplementary Tables 4–6. For $r < 11$ Å, the PDF can be fitted well by the model. However, for interlayer regions ($11 < r < 21.0$ Å), the model starts to deviate from the data. Our results are consistent with the literature reports for pristine VOH, indicating that the intra-layer structure of Ch-VOH and Ch₂-VOH can be well described, but the interlayer turbostratically disordering exits along the c -axis, and the well-ordered interlayer model can only describe about three layers, as by the refined correlation lengths about 4 nm in the Supplementary Table 7. The local structure distortions in Ch-VOH and Ch₂-VOH are confirmed by both the qualitative and quantitative PDF analysis. The PDF data shows that Ch-VOH and Ch₂-VOH are different from the pristine VOH, reflecting changes in the local environment and confirming the successful pre-intercalation of organic cations into the samples. The V₂O₅· n H₂O structure model (Supplementary Fig. 4b), features four oxygen atoms at distances ranging from 1.79 to 2.10 Å forming a plane with the central V atom, while oxygen atoms are with -1.60 Å above and -2.50 Å below the plane of the V atom. The variation in the lengths of these V-O bonds results in distinguishable splitting in the experimental PDF peak at about -1.6 Å (Fig. 2e), demonstrating the sufficient real-space resolution of PDF for detecting-structure changes and distortions in the local atomic environment. The PDF peak positions directly reflect the bond length, and the area underneath peaks are related to the atomic coordination environment. Through the structural simulation of PDF, the influence of varying atomic bond lengths on the peaks becomes distinguishable. The first peak at 1.85 Å corresponds to the V-O bonds, where both Ch-VOH and Ch₂-VOH exhibit deviations from the pristine sample, indicating octahedral distortions in both samples. Particularly, the deviation of V-O bonds in Ch₂-VOH is larger, meaning greater distortion of

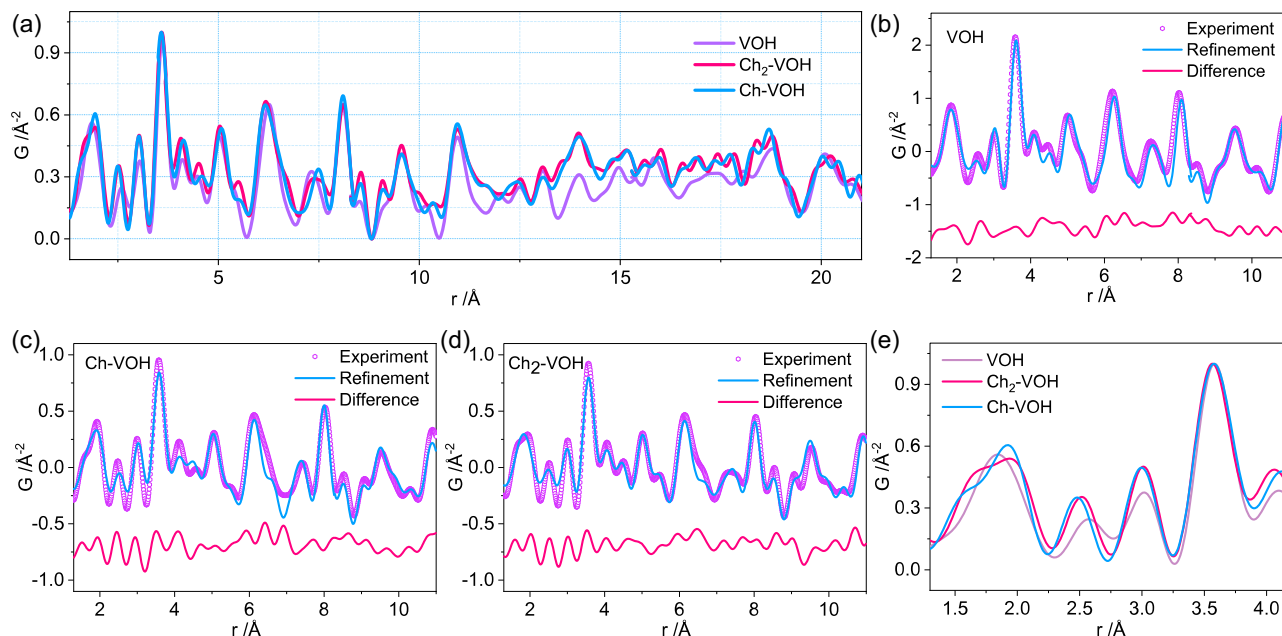


Fig. 2 | Local structure information of VOH, Ch-VOH and Ch₂-VOH. Experiment PDF data for pristine VOH, Ch-VOH, and Ch₂-VOH samples over the range of: (a) 1.3–21.0 Å. The experimental X-ray PDF data are fit by the VOH crystal model over

the range of 1.2 < r < 11 Å: (b) VOH; (c) Ch-VOH; (d) Ch₂-VOH. e The experimental X-ray PDF data at range of 1.3–4.2 Å. The changes of O atoms sites are the primary reason for the structural distortions in Ch-VOH and Ch₂-VOH.

the octahedra. The second peak at 2.53 Å, representing the nearest O-O bonds, which shifts to low- r region for both pre-intercalated samples. The third peak (3.01 Å) mainly arises from the V-V bonds, with a small contribution from the O-O bonds, and the peak in Ch-VOH exhibits slightly decrease. The fourth peak, located at 3.57 Å, mostly originates from V-V pair distances along a and b axes. These V cations form the motif of the octahedra plane, and the PDF analysis reveals that both the position and the area of this peak remain almost unchanged, indicating the interlayer structure motif or skeleton is intact. Therefore, PDF analysis suggests that the changes of O atoms sites are the primary cause of the structural distortions in Ch-VOH and Ch₂-VOH. The comprehensive description of the PDF experiment can be found in the supplementary information (Si).

The aforementioned results confirm that the pre-intercalation of organic cations into the interlayer of VOH, as illustrated in Fig. 3a. And the interaction between pre-inserted cations and oxygen induces a distortion of [VO₆] octahedra (Fig. 3b) and results in the secondary splitting of 3d orbitals as shown in Fig. 3c. Under an ideal octahedral coordination field, the first splitting of 3d orbitals occurs and the five-fold degenerate V 3d orbitals split into lower-energy three-fold degenerate t_{2g} orbitals and higher-energy two-fold degenerate e_g orbitals. Due to the compression along c-axis as verified by EXAFS and PDF analysis, the crystal field repulsion of Ch₂-VOH along the c-axis was increased, leading to a larger secondary splitting energy and lower energy level of the 3d_{xy} orbital compared to Ch-VOH. With nearly the same amount of cations insertion, Ch₂-VOH exhibits a larger lattice spacing, less interlayer water, greater distortion of the [VO₆] octahedra.

X-ray photoelectron spectroscopy (XPS) was used to explore the chemical composition and states of the as-prepared materials with different pre-inserted cations. As shown in Fig. 4a, five peaks in XPS survey spectra correspond to V 1s, O 1s, V 2p, N 1s and C 1s, respectively. Compared to Ch-VOH, the presence of Cl signal in Ch₂-VOH indicates the difference in pre-intercalated cations. In Fig. 4b, the valence band spectra of both samples exhibit a split into two regions. The broad peak centered at around 6 eV is attributed to O 2p, while the narrow and low-intensity region around 1.5 eV belongs to V 3d³⁶. The

occupied V 3d-band width was detected by the X-ray source at approximately 1.5 eV for Ch₂-VOH and 1.4 eV for Ch-VOH. Compared to Ch-VOH, a slight shift towards higher energy in the valence band spectrum of V 3d orbitals in Ch₂-VOH is observed. This shift is attributed to the lowering of the energy level of V 3d_{xy} orbital in Ch₂-VOH caused by the greater distortion of the octahedra. The electrons in 3d_{xy} orbital of Ch₂-VOH are more stable than those in Ch-VOH and require more energy for extraction. Moreover, the O 2p-band of Ch₂-VOH shifts to a lower energy due to the hybridization between V 3d and O 2p³⁷. The high-resolution Cl 2p spectrum of Ch₂-VOH splits into two peaks as shown in Fig. 4c. One peak at 199.3 eV corresponds to C-Cl, and the other at 200.8 eV corresponds to Cl 2p_{1/2}³⁸. In the V 2p spectra (Fig. 4d), two pairs of peaks appear in the range of 513–527 eV, indicative of V⁴⁺ and V⁵⁺, respectively. The peak area ratio of V⁴⁺ in Ch-VOH closes to that of Ch₂-VOH, indicating approximately equal amount of both cations pre-inserted in both samples during the preparation process. In the O 1s spectra (Fig. 4e), two peaks in the range of 526–534 eV for Ch₂-VOH correspond to V-O (529.5 eV) and oxygen vacancies (530.5 eV)³⁹. In addition to the observed peaks of V-O (529.5 eV) and oxygen vacancies (530.4 eV), Ch-VOH exhibits an additional peak at 531.7 eV attributed to interlayer water molecules²⁴, in comparison with Ch₂-VOH. These results suggest that C₅H₁₃N⁺Cl cations are more effective than C₅H₁₃N⁺OH cations in terms of excluding interlayer water, even though the pre-insertion amounts of the two cations are nearly identical. This result supports the analysis from TG-DSC. In the N 1s spectra (Fig. 4f), the signal at around 399.4 and 398.9 eV correspond to C-N bonds from pre-inserted organic cations. Another peak at around 401.5 eV originates from the N-O bonds formed by C₅H₁₃N⁺Cl or C₅H₁₃N⁺OH cations and O in the vanadium oxide layer⁴⁰. This further verifies that the organic cations of C₅H₁₃N⁺Cl or C₅H₁₃N⁺OH are pre-inserted into the VOH lattice, with the chemical bonds forming between N from the organic cations and O within the [VO₆] interlayers of vanadium oxide. Notably, the formation of the N-O bond is beneficial in attenuating the electrostatic attraction between O²⁻ and Zn²⁺ ions. As described above, the pre-insertion of different organic cations regulates the chemical state and adjusts the energy level of 3d orbitals.

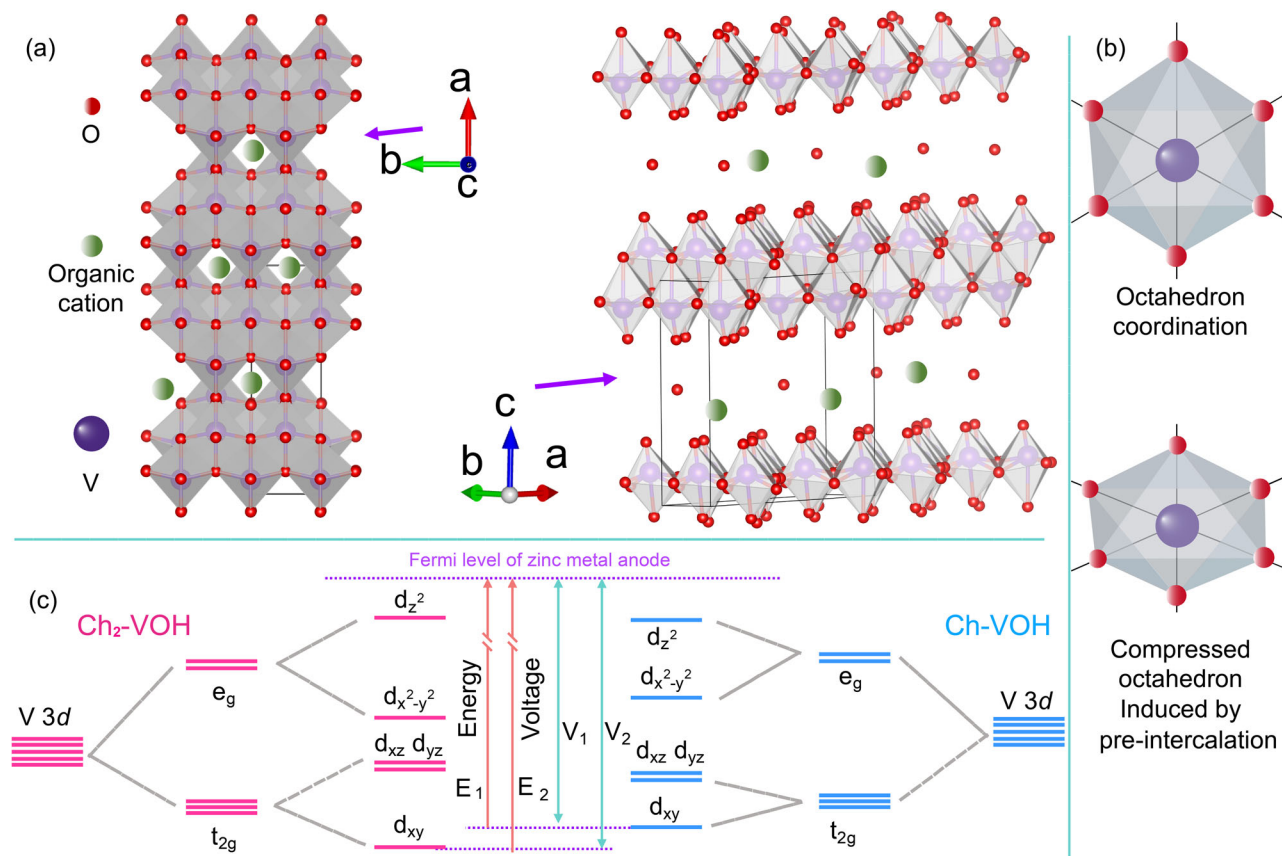


Fig. 3 | Schematic of the structure and orbitals. **a** Organic cations pre-intercalated hydrated vanadate. The crystal structure keeps the original bilayered framework and the cations replace partial water and occupy the sites. **b** The distortion in the $[\text{VO}_6]$ octahedron. Pre-intercalated cation interacts with the oxygen from $[\text{VO}_6]$ octahedra and induce the compression along c-axis as

verified by XAFS and PDF. **c** $3d$ orbitals splitting of vanadium ion in $\text{Ch}_2\text{-VOH}$ and Ch-VOH . The different interaction and distortion in the $[\text{VO}_6]$ octahedra induce the different secondary splitting energy, causing different energy levels in orbitals. The lower energy level of $3d_{xy}$ orbital offers a higher operating voltage in the redox reaction.

Reaction kinetics and electrochemical performance

The electrochemical performance was assessed using a zinc plate as the anode and a 3 M $\text{Zn}(\text{OTf})_2$ ($\text{OTf}^- = \text{CF}_3\text{SO}_3^-$) aqueous solution as the electrolyte. The galvanostatic charge/discharge (GCD) profiles recorded at a specific current of 1 A g^{-1} are shown in Fig. 5a, the clearly visible charge/discharge platforms at 1.1–0.8 V and 0.8–0.3 V are observed in the $\text{Ch}_2\text{-VOH}$ curves, relating to the insertion/extraction of active Zn^{2+} . Importantly, the mid-point voltage of $\text{Ch}_2\text{-VOH}$ is significantly higher than that of Ch-VOH due to the difference in the energy levels of the $3d$ orbitals for the two samples. As discussed above, the $[\text{VO}_6]$ octahedra in $\text{Ch}_2\text{-VOH}$ exhibit greater distortion than those in Ch-VOH , resulting in a larger splitting energy in the $V t_{2g}$ orbitals of $\text{Ch}_2\text{-VOH}$ (Fig. 3c). Consequently, the $3d_{xy}$ orbital of $\text{Ch}_2\text{-VOH}$ demonstrates a stronger electron affinity than that of Ch-VOH , leading to a higher voltage platform compared to Ch-VOH . At the specific currents of 1, 2, 4, and 8 A g^{-1} (Supplementary Fig. 10), the discharging voltage platforms of $\text{Ch}_2\text{-VOH}$ are higher than those of Ch-VOH , confirming the superior voltage outputs in $\text{Ch}_2\text{-VOH}$. The CV contour plots of both samples are shown in Fig. 5b, c. The cathodic peaks at -0.93 V (peak 4) and -0.45 V (peak 3) correspond to the reduction of V^{5+} to V^{4+} and V^{4+} to V^{3+} , respectively. The anodic peaks at -0.73 V (peak 1) and -1.16 V (peak 2) during the anodic sweep originate from the transition from V^{3+} to V^{4+} and V^{4+} to V^{5+} in the charging process. $\text{Ch}_2\text{-VOH}$ cathode shows a higher current response compared with Ch-VOH , especially in the region of $\text{V}^{4+}/\text{V}^{5+}$ transition⁴¹. Meanwhile, with the decrease in scan rates, the current response of the $\text{Ch}_2\text{-VOH}$ cathode remains evident, indicating excellent Zn^{2+} diffusion kinetics. Moreover, $\text{Ch}_2\text{-VOH}$ exhibits a higher response current peak compared

to Ch-VOH , indicating a higher specific capacity. In addition, the open circuit voltage (OCV) of $\text{Ch}_2\text{-VOH}$ is higher than that of Ch-VOH (Fig. 5d) due to the lower energy of $V 3d_{xy}$ orbital of $\text{Ch}_2\text{-VOH}$ than that of Ch-VOH . Galvanostatic intermittent titration technique (GITT) was performed to estimate the Zn^{2+} diffusion coefficients of both samples. The Zn^{2+} diffusion coefficients ($D_{\text{Zn}^{2+}}$) of $\text{Ch}_2\text{-VOH}$ and Ch-VOH , range from 10^{-8} to $10^{-10} \text{ cm}^2 \text{ s}^{-1}$ in Fig. 5e, are superior to those of previously reported vanadium-based cathodes in Zn^{2+} storage^{42,43}. During the discharge process, the $D_{\text{Zn}^{2+}}$ of $\text{Ch}_2\text{-VOH}$ is measured within a range of 5.0×10^{-9} – $6.3 \times 10^{-10} \text{ cm}^2 \text{ s}^{-1}$, while Ch-VOH exhibits a relatively low diffusion coefficient of 3.1×10^{-9} – $4.0 \times 10^{-10} \text{ cm}^2 \text{ s}^{-1}$. Similarly, in the charging process, $\text{Ch}_2\text{-VOH}$ displays a significantly higher $D_{\text{Zn}^{2+}}$ value in comparison to Ch-VOH . It is further verified that the distorted structure of $\text{Ch}_2\text{-VOH}$ caused by the pre-inserted $\text{C}_5\text{H}_{13}\text{N}^+\text{Cl}^-$ enables rapid migration of Zn^{2+} and improves the reaction kinetics. Figure 5f illustrates the rate performance of $\text{Ch}_2\text{-VOH}$ and Ch-VOH , where the specific current is gradually increased from 0.5 to 8 A g^{-1} and subsequently reverted to 0.5 A g^{-1} . At a specific current of 8 A g^{-1} , $\text{Ch}_2\text{-VOH}$ retains 60.3% of its initial capacity measured at specific current of 0.5 A g^{-1} , whereas Ch-VOH is only 57.8%. Moreover, the discharge capacity of $\text{Ch}_2\text{-VOH}$ recovers to 404 mA h g^{-1} when the specific current returns to 0.5 mA g^{-1} , suggesting its excellent rate capability. The energy efficiency of $\text{Ch}_2\text{-VOH}$ is evidently higher than that of Ch-VOH (Fig. 5g). The enhanced efficiency is attributed to the higher average voltage and rapid ion diffusion of $\text{Ch}_2\text{-VOH}$ acquired by the modulation of local chemical coordination. Figure 5h shows the cycling performance at a current density of 4 A g^{-1} . The maximum capacity of $\text{Ch}_2\text{-VOH}$ and Ch-VOH batteries reach $285.6 \text{ mA h g}^{-1}$ and $285.9 \text{ mA h g}^{-1}$, respectively,

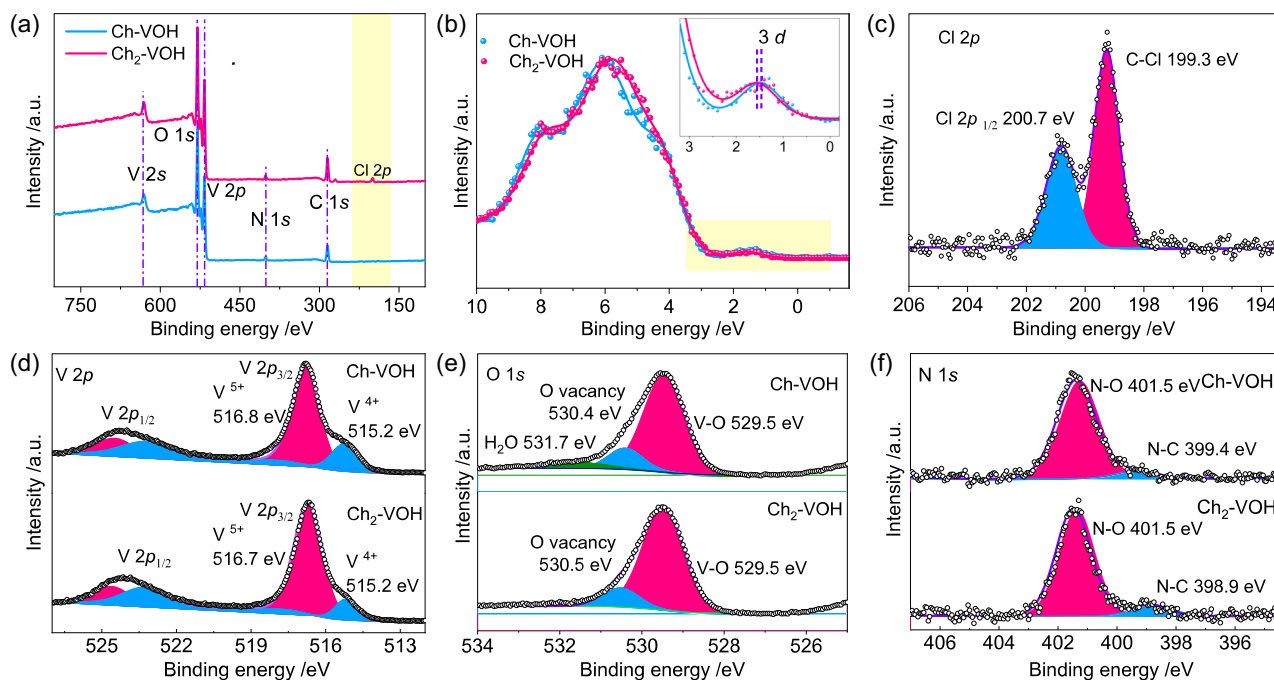


Fig. 4 | Chemical states of elements and valence bands of both samples. **a** XPS survey spectra. The signal from element Cl verifies the difference of intercalants. **b** Valence band spectra. The occupied V 3d band in Ch₂-VOH presents a slight shift toward high binding energy because of the lower energy level of d_{xy} after the secondary splitting. **c** High resolution spectrum of Cl 2p collected from Ch₂-VOH. It confirms the C-Cl connection in the molecular chain. **d** V 2p spectra. Organic

intercalants introduce V⁴⁺ in both lattices because of charge balance, confirming the successful pre-intercalation. **e** O 1s spectra. The detected water signal suggests a more competitive expulsion from C₅H₁₃N⁺Cl on lattice water compared to C₅H₁₃N⁺OH. **f** N 1s spectra. The presence of C-N bonds from the skeletons of organic cations and the formation of N-O bonds suggest the strong chemical interaction between the intercalants and the lattice oxygen.

after the period of activation caused by electrolyte penetration. After 1000 cycles, the capacity of the Ch₂-VOH battery shows almost no attenuation, maintaining an impressive 98.8% of its maximum capacity. In contrast, the capacity of the Ch-VOH battery decays to 241 mA h g⁻¹, retaining 85.6% of its maximum capacity. In comparison to other reported cathode materials^{19,44,45}, Ch₂-VOH exhibits excellent cycling life and Zn²⁺ diffusion kinetics. Overall, Ch₂-VOH cathode presents higher open circuit and operating voltages, and preferable electrochemical reversibility as well as better cycling stability, which are attributed to the distorted [VO₆] octahedra and open structure generated by C₅H₁₃N⁺Cl cations pre-intercalation.

In summary, this work establishes a model linking the local chemical coordination and electron orbital occupation with electrochemical performance on the basis of crystal field theory. V₂O₅·nH₂O pre-intercalated with chlorcholine cation with a greater local distortion achieves excellent Zn²⁺ diffusion kinetics and elevated operating voltage as well as enhanced cycling stability in comparison with pre-intercalated choline cation. These enhancements attribute to the induced distortion in octahedral coordination field of vanadium. The t_{2g} orbitals of Ch₂-VOH exhibit higher secondary splitting energy and the $3d_{xy}$ orbital possesses a lower energy level. Thereby, it elevates the open circuit voltage from 1.55 V to 1.68 V, and the mid-point voltage presents an increase of 50 mV. In addition, the strong interaction between the organic cation and oxygen from the [VO₆] octahedra stabilize the bi-layered structure of hydrated vanadate, achieving an impressive capacity retention of 98.8% at specific current of 4 A g⁻¹ over 1000 cycles. This work provides insightful guidance for the voltage regulation in the cathode materials of rechargeable batteries.

Methods

Synthesis of samples

All chemicals were used as received without further purification steps.

To prepare the samples, 2 mmol of V₂O₅ (99.6 + %, supplier: Sigma-Aldrich) was dissolved in 50 mL of deionized water (DI H₂O) with 2 mL of H₂O₂ (30%, supplier: Aladdin). Separately, 1 mmol of C₅H₁₃Cl₂N or C₅H₁₄CINO (supplier: Aladdin) was dissolved in 30 mL of DI water. Two solutions were mixed and filled into a 100 mL of Teflon lined stainless steel autoclave (internal diameter: 42 mm, height: 72 mm), then heated and maintained at 120 °C for 6 h.

Afterward, the precipitates were obtained by centrifugation, followed by washing with water and ethanol three times. The collected precipitates were dried overnight in an electric oven at 70 °C, resulting in greenish powders. The resulting products were further dried at 120 °C in a vacuum oven for 2 h.

Preparation of cathode host and battery assembly

For electrode preparation, the active material, conductive carbon, and polyvinylidene fluoride (PVDF) binder were mixed with a weight ratio of 7:2:1 in N-methyl-2-pyrrolidone (NMP) solvent to produce a slurry. This slurry was coated onto a titanium foil serving as the current collector. The resulting electrodes were subsequently dried in a vacuum oven at 60 °C overnight. The active material was loaded onto the electrodes at a density ranging from 1 to 2 mg/cm². To prepare coin batteries (2032 type with 316 stainless steel), Zn metal disc was utilized as the anode with a diameter of 14 mm, and the batteries were filled with 80 μL of 3 M Zn(Otf)₂ aqueous solution as the electrolyte. Separator between electrodes was a glass fiber filter of Whatman, Grade GF/A.

Characterizations

The crystal structure of the samples was identified by Cu K α radiation X-ray diffraction (XRD, SmartLab, 3 kW). The bonding properties of the samples were analyzed by Fourier transform infrared (FT-IR, Bruker ALPHA) absorption spectroscope and Raman spectroscope (Thermo

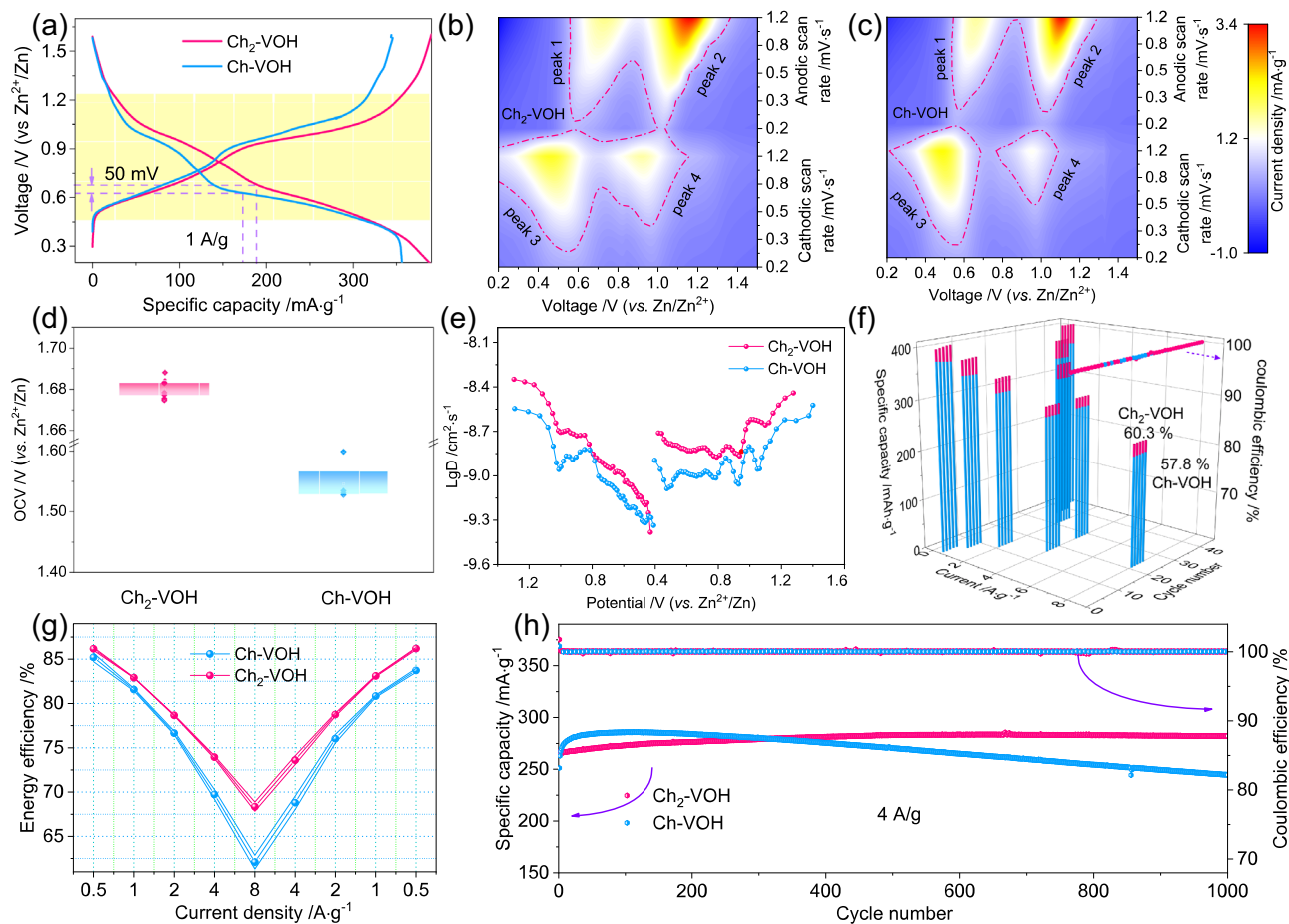


Fig. 5 | Electrochemical properties Ch₂-VOH and Ch-VOH cathodes in aqueous zinc ion batteries. **a** The GCD curve at a specific current of 1 A g⁻¹. CV contour of **(b)** Ch₂-VOH and **(c)** Ch-VOH. The larger area and stronger intensity at the same scan rate reflect Ch₂-VOH with better reaction kinetics. **d** Open circuit voltage. The higher midpoint voltage and OCV of Ch₂-VOH verify the impacts of local coordination manipulation. **e** Zn²⁺ diffusion coefficients. The Zn²⁺ diffusion coefficients of Ch₂-VOH are higher than that of Ch-VOH in the charging and discharging process

under a specific current of 50 m A g⁻¹. **f** Rate performance. The enhanced capacities of Ch₂-VOH at high current densities are offered by the fast ion diffusion and charge transfer. **g** Energy efficiency at the different current densities. The smaller polarization from fast mass transfer enables the higher energy efficiencies. **h** Cycling performance at specific current of 4 A g⁻¹. The crystal structure of Ch₂-VOH become more robust in comparison with Ch-VOH.

Scientific DXR 2xi Micro-Raman). Transmission electron microscopy images were obtained by transmission electron microscope (TEM, JEOL, 3200FS) with an accelerating voltage of 300 kV. X-ray photoelectron spectroscopy (XPS, ESCALAB 250Xi) were used to collect the surface chemical states of the samples. The experimental PDF data are carried out at BL08W at Super Photon ring-8 GeV (SPring-8) in Japan. The soft-XAS of the V L-edge and O K-edge was performed by National Synchrotron Radiation Research Center (NSRRC) in Taiwan at BL20A1 beamline. V K-edge X-ray absorption spectra were collected using an easyXAFS300+ benchtop instrument (easyXAFS, LLC), using a Ge (211) ball-bending crystal analyzer and an Ag anode X-ray tube. Spectra were deadtime corrected and energy were calibrated using a standard V metal foil. Thermogravimetry - differential scanning calorimetry (TG-DSC) analysis was conducted by Jupiter Netzsch, 449F3 with a temperature range of 40–700 °C in a flowing of Air. Electron Paramagnetic Resonance (EPR) was performed by a Bruker A300 spectrometer.

Electrochemical measurements

All electrochemical measurements were conducted at 25 °C and at the voltage range of 0.2–1.6 V. The redox reactions of the cathodes were detected by cyclic voltammetry (CV). In addition, the galvanostatic intermittent titration technique (GITT) and galvanostatic charge and discharge assessments were used to analyze reaction kinetics and cycling stability on a Neware tester (MIHW-200-160CH-B). GITT tests

were carried out at a current density of 50 milliamperes per gram and involved a charge/discharge duration of 10 min for each step.

Reporting summary

Further information on research design is available in the Nature Portfolio Reporting Summary linked to this article.

Data availability

The data that support the plots in this paper and its Supplementary Information are available. All other relevant data that support the findings of this study are available from the corresponding authors on reasonable request. The source data underlying Figs. 1, 2, 4 and 5, Supplementary Figs. 2, 3, Supplementary Figs. 5–10 are provided in the Source Data file. Source data are provided with this paper.

References

- Jia, X., Liu, C., Neale, Z. G., Yang, J. & Cao, G. Active materials for aqueous zinc ion batteries: synthesis, crystal structure, morphology, and electrochemistry. *Chem. Rev.* **120**, 7795–7866 (2020).
- Ming, J., Guo, J., Xia, C., Wang, W. & Alshareef, H. N. Zinc-ion batteries: materials, materials, mechanisms, and applications. *Mater. Sci. Eng., R.* **135**, 58–84 (2019).
- Zhang, N. et al. Materials chemistry for rechargeable zinc-ion batteries. *Chem. Soc. Rev.* **49**, 4203–4219 (2020).

- Yu, X. et al. Ten concerns of Zn metal anode for rechargeable aqueous zinc batteries. *Joule* **7**, 1145–1175 (2023).
- Ma, L. et al. Realizing high zinc reversibility in rechargeable batteries. *Nat. Energy* **5**, 743–749 (2020).
- Ye, X. et al. Unraveling the deposition/dissolution chemistry of MnO₂ for high-energy aqueous batteries. *Energy Environ. Sci.* **16**, 1016–1023 (2023).
- Ma, L. et al. Achieving high-voltage and high-capacity aqueous rechargeable zinc ion battery by incorporating two-species redox reaction. *Adv. Energy Mater.* **9**, 1902446 (2019).
- Wang, H., Wu, Q., Cheng, L. & Zhu, G. The emerging aqueous zinc-organic battery. *Coord. Chem. Rev.* **472**, 214772 (2022).
- Ye, J. J. et al. Manipulating oxygen vacancies to spur ion kinetics in V₂O₅ structures for superior aqueous zinc-ion batteries. *Adv. Funct. Mater.* **33**, 2305659 (2023).
- Lv, T. et al. Co-intercalation of dual charge carriers in metal-ion-confining layered vanadium oxide nanobelts for aqueous zinc-ion batteries. *Angew. Chem. Int. Ed.* **62**, e202216089 (2022).
- Hou, Z. et al. Eliminating the Mn 3d orbital degeneracy to suppress the Jahn-Teller distortion for stable MnO₂ cathode. *Adv. Energy Mater.* **14**, 2302477 (2023).
- De Jesus, L. R. et al. Mapping polaronic states and lithiation gradients in individual V₂O₅ nanowires. *Nat. Commun.* **7**, 12022 (2016).
- Ma, L. et al. Achieving both high voltage and high capacity in aqueous zinc-ion battery for record high energy density. *Adv. Funct. Mater.* **29**, 1906142 (2019).
- Wang, T. et al. Ultrafast 3D hybrid-ion transport in porous V₂O₅ cathodes for superior-rate rechargeable aqueous zinc batteries. *Adv. Energy Mater.* **13**, 2204358 (2023).
- Wang, X. et al. Pseudocapacitive zinc cation intercalation with superior kinetics enabled by atomically thin V₂O₅ nanobelts for quasi-solid-state microbatteries. *Energy Storage Mater.* **50**, 454–463 (2022).
- Ma, X. et al. Organic-inorganic hybrid cathode with dual energy-storage mechanism for ultrahigh-rate and ultralong-life aqueous zinc-ion batteries. *Adv. Mater.* **34**, 2105452 (2021).
- Wan, F. et al. A universal compensation strategy to anchor polar organic molecules in bilayered hydrated vanadates for promoting aqueous zinc-ion storage. *Adv. Mater.* **33**, 2102701 (2021).
- Liu, H. et al. Van der Waals interaction-driven self-assembly of V₂O₅ nanoplates and MXene for high-performing zinc-ion batteries by suppressing vanadium dissolution. *ACS Nano* **16**, 14539–14548 (2022).
- Liu, Y. et al. Pre-intercalation chemistry of electrode materials in aqueous energy storage systems. *Coord. Chem. Rev.* **460**, 214477 (2022).
- Liu, C. et al. Expanded hydrated vanadate for high-performance aqueous zinc-ion batteries. *Energy Environ. Sci.* **12**, 2273–2285 (2019).
- Liu, H. et al. Fast zinc-ion storage enabled by hydrophobic alkyl chains via reducing dual diffusion barriers. *Energy Storage Mater.* **65**, 103092 (2024).
- Qiu, N. et al. Toward a high-performance aqueous zinc ion battery: Potassium vanadate nanobelts and carbon enhanced zinc foil. *Nano Lett.* **21**, 2738–2744 (2021).
- Kundu, D., Adams, B. D., Duffort, V., Vajargah, S. H. & Nazar, L. F. A high-capacity and long-life aqueous rechargeable zinc battery using a metal oxide intercalation cathode. *Nat. Energy* **1**, 16119 (2016).
- Li, R. et al. Intercalated polyaniline in V₂O₅ as a unique vanadium oxide bronze cathode for highly stable aqueous zinc ion battery. *Energy Storage Mater.* **38**, 590–598 (2021).
- Sun, J. et al. “Three-in-one” strategy that ensures V₂O₅·nH₂O with superior Zn²⁺ storage by simultaneous protonated polyaniline intercalation and encapsulation. *Small Struct.* **3**, 2100212 (2022).
- Ye, K. et al. An overview of advanced methods for the characterization of oxygen vacancies in materials. *TrAC, Trends Anal. Chem.* **116**, 102–108 (2019).
- Wang, J. et al. CaV₆O₁₆·2.8H₂O with Ca²⁺ pillar and water lubrication as a high-rate and long-life cathode material for Ca-ion batteries. *Adv. Funct. Mater.* **32**, 2113030 (2022).
- Sun, Q. et al. Uncovering the fundamental role of interlayer water in charge storage for bilayered V₂O₅·nH₂O xerogel cathode materials. *Adv. Energy Mater.* **13**, 2202515 (2022).
- Sarang, R. X-ray absorption near-edge spectroscopy in bioinorganic chemistry: application to M-O₂ systems. *Coord. Chem. Rev.* **257**, 459–472 (2013).
- Wang, X. et al. Pivotal role of reversible NiO₆ geometric conversion in oxygen evolution. *Nature* **611**, 702–708 (2022).
- Ravel, B. & Newville, M. Athena, Artemis, Hephaestus: data analysis for X-ray absorption spectroscopy using ifeffit. *J. Synchrotron Radiat.* **12**, 537–541 (2005).
- Petkov, V. et al. Structure of V₂O₅·nH₂O xerogel solved by the atomic pair distribution function technique. *J. Am. Chem. Soc.* **124**, 10157–10162 (2002).
- Avansi, W., Maia, L. J. Q., Ribeiro, C., Leite, E. R. & Mastelaro, V. R. Local structure study of vanadium pentoxide 1D-nanostructures. *J. Nanopart. Res.* **13**, 4937–4946 (2011).
- Abbate, M. et al. Soft X-ray absorption spectroscopy of vanadium oxides. *J. Electron. Spectrosc. Relat. Phenom.* **62**, 185–195 (1993).
- Fischer, D. W. Molecular-orbital interpretation of the soft X-ray L_{II, III} emission and absorption spectra from some titanium and vanadium compounds. *J. Appl. Phys.* **41**, 3561–3569 (1970).
- Sawatzky, G. A. & Post, D. X-ray photoelectron and auger spectroscopy study of some vanadium oxides. *Phys. Rev. B* **20**, 1546–1555 (1979).
- Wang, F. et al. A rechargeable aqueous Zn²⁺-battery with high power density and a long cycle-life. *Energy Environ. Sci.* **11**, 3168–3175 (2018).
- Hoste, S., Van De Vondel, D. F. & Van Der Kelen, G. P. XPS spectra of organometallic phenyl compounds of P, As, Sb and Bi. *J. Electron. Spectrosc. Relat. Phenom.* **17**, 191–195 (1979).
- Jia, X., Liu, C., Wang, Z., Huang, D. & Cao, G. Weakly polarized organic cation-modified hydrated vanadium oxides for high-energy efficiency aqueous zinc-ion batteries. *Nano-Micro Lett.* **16**, 129 (2024).
- Tong, Y. et al. Synergistic iron ion and alkylammonium cation intercalated vanadium oxide cathode for highly efficient aqueous zinc ion battery. *J. Power Sources* **528**, 231226 (2022).
- Liu, S. et al. Tuning the kinetics of zinc-ion insertion/extraction in V₂O₅ by in situ polyaniline intercalation enables improved aqueous zinc-ion storage performance. *Adv. Mater.* **32**, 2001113 (2020).
- Deng, S. et al. Electrochemically induced metal-organic-framework-derived amorphous V₂O₅ for superior rate aqueous zinc-ion batteries. *Angew. Chem. Int. Ed.* **59**, 22002–22006 (2020).
- Zhang, S. et al. Boosting zinc-ion storage in vanadium oxide via “dual-engineering” strategy. *Nano Energy* **115**, 108736 (2023).
- Zhu, J. et al. A molecular-sieve electrolyte membrane enables separator-free zinc batteries with ultralong cycle life. *Adv. Mater.* **34**, 2207209 (2022).
- Zhu, M. et al. A fluorinated solid-state-electrolyte interface layer guiding fast zinc-ion oriented deposition in aqueous zinc-ion batteries. *Angew. Chem. Int. Ed.* **63**, e202316904 (2023).

Acknowledgements

This work is financially supported by the National Natural Science Foundation of China (Grant No. 52102277 to C.L.) and the Fundamental Research Funds for the Central Universities, conducted by Tongji University. Dr. Liu appreciates the XAFS technique support by Dr. Jingpeng Zhao from Quantum Design China. Research facilities of soft-XAS was

provided by the beamline of TLS BL20A1, National Synchrotron Radiation Research Center (NSRRC) in Taiwan. The synchrotron radiation PDF experiments were performed at BL08W of SPring-8 with the approval of Japan Synchrotron Radiation Research Institute (JASRI, Proposal No. 2023A1347). Dr. Yang thanks the staff of beamline BL13SSW at Shanghai Synchrotron Radiation Facility for X-ray PDF experiment supports.

Author contributions

C.L., Y.P., and G.C. conceived the concept. H.L. and H.N. performed all electrochemical performance tests. H.N. performed all data analyses and wrote the manuscript. L.Y. and T.K. performed PDF tests and data analyses. B.J. performed wavelet transform data analyses. W.H. and C.C. performed the soft XAS test. T.S., Y.P., G.C. and C.L. revised the manuscript, and all authors contributed to the manuscript.

Competing interests

The authors declare no competing interests.

Additional information

Supplementary information The online version contains supplementary material available at <https://doi.org/10.1038/s41467-024-53785-2>.

Correspondence and requests for materials should be addressed to Yanzhong Pei, Guozhong Cao or Chaofeng Liu.

Peer review information *Nature Communications* thanks the anonymous reviewers for their contribution to the peer review of this work. A peer review file is available.

Reprints and permissions information is available at <http://www.nature.com/reprints>

Publisher's note Springer Nature remains neutral with regard to jurisdictional claims in published maps and institutional affiliations.

Open Access This article is licensed under a Creative Commons Attribution-NonCommercial-NoDerivatives 4.0 International License, which permits any non-commercial use, sharing, distribution and reproduction in any medium or format, as long as you give appropriate credit to the original author(s) and the source, provide a link to the Creative Commons licence, and indicate if you modified the licensed material. You do not have permission under this licence to share adapted material derived from this article or parts of it. The images or other third party material in this article are included in the article's Creative Commons licence, unless indicated otherwise in a credit line to the material. If material is not included in the article's Creative Commons licence and your intended use is not permitted by statutory regulation or exceeds the permitted use, you will need to obtain permission directly from the copyright holder. To view a copy of this licence, visit <http://creativecommons.org/licenses/by-nc-nd/4.0/>.

© The Author(s) 2024